International Journal of Nanomedicine

Dovepress

open access to scientific and medical research

Open Access Full Text Article

ORIGINAL RESEARCH

Photocatalytic Cu_2WS_4 Nanocrystals for Efficient Bacterial Killing and Biofilm Disruption

Heng Dong[1,*], Kaili Yang[2,*], Yu Zhang[1], Qiang Li[1], Weijun Xiu[2], Meng Ding[1], Jingyang Shan[3], Yongbin Mou[1]

[1]Nanjing Stomatological Hospital, Medical School of Nanjing University, Nanjing, People's Republic of China; [2]Key Laboratory for Organic Electronics and Information Displays & Jiangsu Key Laboratory for Biosensors, Institute of Advanced Materials (IAM), Jiangsu National Synergetic Innovation Centre for Advanced Materials (SICAM), Nanjing University of Posts and Telecommunications, Nanjing, People's Republic of China; [3]Department of Neurology, Shenzhen Institute of Translational Medicine, The First Affiliated Hospital of Shenzhen University, Shenzhen Second People's Hospital, Shenzhen, 518000, People's Republic of China

*These authors contributed equally to this work

Correspondence: Yongbin Mou, Nanjing Stomatological Hospital, Medical School of Nanjing University, #30 Zhongyang Road, Nanjing, 210008, People's Republic of China, Email yongbinmou@163.com; yongbinmou@nju.edu.cn; Jingyang Shan, Department of Neurology, Shenzhen Institute of Translational Medicine, The First Affiliated Hospital of Shenzhen University, Shenzhen Second People's Hospital, Shenzhen, 518000, People's Republic of China, Email jyshandr@163.com

Background: Bacterial biofilm-related wound infections threaten human health due to the lack of efficient treatments. Therefore, developing a novel strategy for wound infection care is urgently needed.

Methods: Cube-shaped Cu_2WS_4 nanocrystals (CWSNs) were successfully prepared via a microwave-assisted method. CWSNs, as photocatalysts, were first studied by using fluorescence spectroscopy for their ability to generate reactive oxygen species (ROS). The antibacterial and biofilm inhibition abilities of CWSNs were determined in vitro by using *Staphylococcus aureus* (*S. aureus*) as the model bacterium. Moreover, a CWSN gel was prepared and applied to treat *S. aureus*-infected wounds in mice. The toxicity of the CWSNs was evaluated through in vitro cell and in vivo animal experiments.

Results: Studies on the properties of the CWSNs demonstrated that these nanomaterials can catalyze the generation of hydroxyl radicals (•OH) without the addition of H_2O_2 after visible-light irradiation, indicating their photocatalytic ability. Moreover, the in vitro experimental results showed that the CWSNs not only adhered to the surfaces of *S. aureus* to kill the bacteria, but also inhibited *S. aureus* biofilm formation. The in vivo study showed that the CWSN gel produced excellent antibacterial effects against *S. aureus* infected wounds in mice and effectively promoted wound healing. Furthermore, toxicity tests showed that the CWSNs have negligible toxicity in vitro and in vivo.

Conclusion: This work provides a potential photocatalytic antibacterial nanoagent for efficient bacterial killing, inhibition of biofilms growth and wound infection treatment.

Keywords: Cu_2WS_4 nanocrystals, *Staphylococcus aureus*, visible light, hydroxyl radical, antibacterial, biofilms

Introduction

Antibiotic-resistant bacteria have become both a worldwide problem and major hidden danger that threatens global public health. Currently, the abuse of antibiotics is a particularly serious problem, often leading to the emergence of drug-resistant bacteria and even "superbacteria", such as *Staphylococcus aureus* (*S. aureus*).[1,2] Bacterial infections are very challenging to treat, as the actions and penetration of antibiotics are largely limited by the dormant lifestyle of bacteria and the extracellular polymeric substance (EPS) matrix in bacterial biofilms.[3,4] Bacterial biofilms with an EPS matrix can resist host immune defenses and induce persistent inflammation, thus allowing the bacteria to become highly resistant to traditional antibiotics.[5] Ineffective treatment with traditional antibiotics not only causes the rapid emergence of drug-resistant *S. aureus* strains but could also result in the formation of S. *aureus* biofilms.[6] Therefore, the development of a new strategy to inhibit *S. aureus* biofilm formation is urgently needed.

Received: 3 February 2022
Accepted: 15 June 2022
Published: 22 June 2022

Graphical Abstract

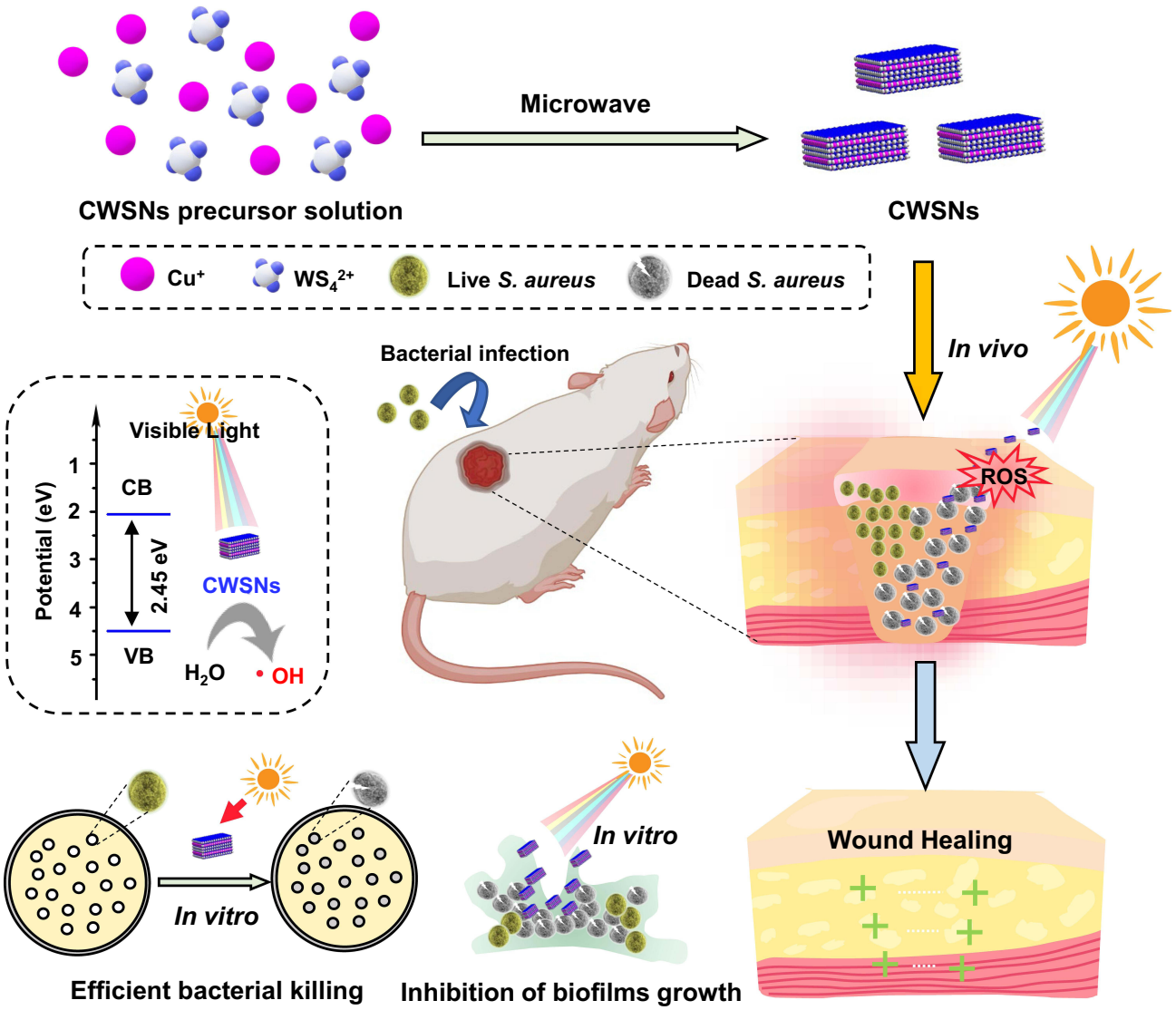

With advances in nanotechnology, nanomaterials have been considered for antibacterial applications.[7–11] To date, photocatalysts that utilize different parts of the solar spectrum have been widely investigated. When photocatalytic nanomaterials absorb visible-light and generate electron-hole pairs, the electrons and holes can react with water and dissolved oxygen separately to generate a myriad of reactive oxygen species (ROS).[12] These ROS can react with proteins, lipids, polysaccharides and other constituents of bacteria, leading to oxidative damage to the bacterial membrane.[13] Compared to the normal hydrogen electrode at pH 7, the potential for ROS production by water oxidation at the hole side are 1.1~1.9 V (water/hydroxyl radicals, $H_2O/•OH$).[14] Therefore, the bandgap of nanomaterials is a key factor that affects the photocatalytic generation of ROS. Furthermore, many nanomaterials, when acting as photocatalysts, induce bactericidal effects through the photocatalytic generation of ROS.[14,15] Notably, photocatalysis is important in the prevention of bacterial biofilm formation, showing great potential against even antibiotic-resistant bacteria. Developing antibacterial nanomaterials that possess certain characteristics such as high antibacterial activity, low toxicity,

and photo-responsiveness remains a great challenge. Cu_2WS_4 is a typical layered ternary chalcogenide with unique physical and chemical properties that are conducive to various applications in supercapacitors and hydrogen evolution.[16,17] A previous study demonstrated that the Cu_2WS_4 catalyst has both enzyme-like (oxidase and peroxidase) properties and selective bacteria-binding abilities, which can facilitate the production of ROS to kill bacteria.[18] However, the antibacterial mechanism and antibiofilm applications of Cu_2WS_4 nanomaterials have not been fully explored.

In the present study, we constructed small (~20 nm), cubic-shaped Cu_2WS_4 nanocrystals (CWSNs) that showed excellent bacteria-binding ability and efficiency inactivated free bacteria at 2 μg/mL under visible-light. In addition, the current study also focused on the interaction relationship between the photocatalytic performance and antibiofilm properties of these CWSNs. The *S. aureus* biofilms were reduced up to ~97% at 200 μg/mL CWSNs under visible-light irradiation, while the biofilms were reduced up to only ~46% at 200 μg/mL CWSNs in the dark. The therapeutic efficacy of the CWSNs against *S. aureus*-infected wounds was investigated in vivo, and the CWSN gel efficiently treated these wounds and promoted wound healing. Our work reveals that photocatalytic CWSNs with good biocompatibility can be highly efficient antibacterial nanoagents for maximizing bacterial infection treatment after their administration under visible-light.

Materials and Methods

Preparation and Characterization of the CWSNs

The CWSNs were prepared by using $(NH_4)_2WS_4$, CuBr and 3-mercaptopropionic acid according to a reported method.[18] The morphology of the CWSNs was characterized by transmission electron microscopy (TEM, HT7700, Hitachi, Japan, 100 kV) and high resolution TEM (HRTEM, F200X, Talos, USA, 200 kV) with energy-dispersive spectrometry X-ray spectroscopy (EDS). X-ray diffraction (XRD) patterns were recorded on a diffractometer (D8 Advance A25, Bruker, Germany) with Cu Kα radiation. Zeta potentials were determined on a Malvern Zetasizer Nanoseries (Nano ZS90). The bandgap of the CWSNs was calculated by the obtained ultraviolet visible near-infrared (UV-vis-NIR) absorption spectrum using a UV-vis-NIR spectrophotometer (UV-3600, Shimadzu, Japan). The valence band (VB) was measured by ultraviolet photoelectron spectroscopy (UPS; Thermo, ESCALAB 250XI, USA).

Hydroxyl Radical Detection

The •OH can react with terephthalic acid (TA) to form the fluorescent compound 2-hydroxyl TA. Two experimental groups (TA (5 mM) and CWSNs (100 μg/mL) + TA) were incubated at room temperature for 2 h. Afterward, the fluorescence of 3 mL of each of the mixtures was measured with a fluorescence spectrophotometer using 312 nm as the excitation wavelength (FluoroMax Plus spectrophotometer, HORIBA, America).

Bacterial Culture

Luria-Bertani (LB) broth (ST156) and LB broth with agar (ST158) were purchased from Beyotime Institute of Biotechnology (Shanghai, China). *S. aureus* (ATCC 25923) and methicillin-resistant *Staphylococcus aureus* (MRSA, ATCC 43300) were revived and streaked on LB agar plates, which were incubated at 37°C for 12 h. A single colony of *S. aureus* or MRSA was selected and used to inoculate 5 mL of LB broth overnight at 37°C with shaking at 220 rpm. The bacterial dispersion was washed with saline, and the optical density (OD) of 600 nm was quantified with a microplate reader. An OD600 = 0.1 indicated that the concentration of *S. aureus* was ~10^8 CFU/mL.

Bacteria-Binding Ability of CWSNs

Bacterial suspensions (3 mL, ~10^7 CFU/mL) were mixed with CWSNs (final concentration 2 μg/mL) in a 15 mL centrifuge tube at 37°C for 2 h. Saline was used as the control. After the different treatments, the bacterial cells were washed three times. After removing the supernatant, TEM samples were prepared according to a previous method.[18] TEM, high resolution-TEM (HRTEM), EDS, and the corresponding element mapping analyses were conducted with a JEM-F200 (URP) electron microscope.

CWSN Bactericidal Effect Assessment

Antibacterial assay of *S. aureus: S. aureus* were washed and diluted to 2×10^6 CFU/mL by using phosphate buffer. CWSNs (2 μg/mL) were incubated with diluted *S. aureus* (2×10^6 CFU/mL) at 37°C (1 or 2 h, with or without visible-light irradiation). The mixtures were diluted 10^1-, 10^2-, 10^3-, and 10^4-fold with saline, and 10 μL of each dilution was dripped onto LB agar plates. After incubation for 18 h at 37°C, the number of CFU was counted. All assays were performed in triplicate.

MRSA antibacterial assay: MRSA were washed and diluted to 2×10^6 CFU/mL by using phosphate buffer. CWSNs (2 μg/mL) were incubated with diluted MRSA (2×10^6 CFU/mL) at 37°C (1 or 2 h, with or without visible-light irradiation). Phosphate buffer and 2 μg/mL vancomycin (Van) were used as controls. The mixtures were diluted 10^3-fold with saline, and 100 μL of each mixture was spread onto LB agar plates. After incubation for 18 h at 37°C, the number of CFUs was counted. All assays were performed in triplicate.

S. aureus Biofilm Formation Inhibition Assay

S. aureus was diluted to 2×10^7 CFU/mL by using LB broth with 1% glucose. Briefly, 100 μL of CWSNs at different concentrations (final concentrations: 1, 10, 100, and 200 μg/mL) was placed to each well of a 96-well plate, and then 100 μL of *S. aureus* suspension was added into each well. The samples were incubated at 37°C under visible-light for 24 h. Another 96-well plate, which was treated in the same manner, was covered with aluminum foil to avoid visible-light illumination to study the antibiofilm activity in the dark. All assays were performed in triplicate.

Crystal Violet Staining Assay

The crystal violet assay was used to quantificationally evaluate the total biofilm biomass. The LB medium of all wells was aspirated, and the contents of the wells were washed two times with saline. The biofilms were fixed with 2.5% glutaraldehyde for 30 min and stained with 0.2% crystal violet at room temperature for 30 min. The excess stain from each well was removed and the contents of the wells were again washed with saline. Next, the crystal violet-stained biofilms were quantified by adding 200 μL of 95% ethanol. For staining, the *S. aureus* biofilms were fixed with formalin for 10 min and stained with crystal violet solution (0.02%) for 1 h. Images were captured with a motorized fluorescence microscope (Olympus IX71). All assays were performed in triplicate.

Biofilm Morphology Analysis

S. aureus was diluted to 2×10^6 CFU/mL by using LB broth with 1% glucose. Briefly, 1 mL of CWSNs at different final concentrations (1, 10, 100, and 200 μg/mL) was placed into confocal dishes, and then 1 mL of *S. aureus* suspension containing glucose was added to each well. The samples were incubated at 37°C for 24 h. The excess medium in confocal dishes was removed, and the biofilms were stained with Calcein-AM at room temperature for 30 min and washed with saline to remove excess stain. Confocal laser scanning microscopy (CLSM) was used to obtain 630×630 μm images (Olympus IX81).

Viability of the Bacteria in the Biofilms

S. aureus suspensions (2×10^7 CFU/mL) in LB broth containing 1% glucose were incubated with 1 mL of different final concentrations of CWSNs (1, 10, 100, and 200 μg/mL) at 37°C for 24 h. Saline was used as a control. The LB medium of each well was removed, and 200 μL of saline was added to each well. Next, the bacterial suspensions were transferred to 1.5 mL tubes containing 800 μL of saline and were collected by ultrasonication for 5 min at room temperature. The mixtures were diluted 1~10^6-fold with saline, and then 100 μL of each mixture was spread onto LB agar plates. After incubation for 18 h at 37°C, the number of CFUs was counted. All assays were performed in triplicate.

Preparation of the Gel and Detection of Its Antibiofilm Potential in vitro

Gel (3% agar) was heated to 45°C, and saline or CWSNs were added. Then, each mixture was cooled to room temperature to obtain the saline gel and CWSN gel. *S. aureus* was diluted to 1×10^6 CFU/mL in agar plates with LB

containing 1% glucose. Then, 50 μL of saline gel or CWSN gel was placed on the plates, and the plates were maintained and observed for 24 h at 37°C.

Mice and Ethics Statement

Specific pathogen-free female BALB/c mice (6~8 weeks, 18~22 g) were purchased from the Qinglong Mountain Company of China. All research procedures were approved by the Animal Care and Use Committee of the Medical School of Nanjing University.

Wound Infection Treatment

The infected wound animal model was generated with *S. aureus* in BALB/c mice. After the dorsal hair was removed from the backs of the mice and a circular defect (d = 4 mm) was created with surgical scissors, all wounds were infected within 24 h by using 100 μL of *S. aureus* suspension (1×10^7 CFU/mL). After the infected wounds were established, the mice were randomly placed into two groups (n = 6/group). The infected mice were treated with saline gel (0.3% agar) or CWSN gel containing 0.3% agar (50 μg/mL CWSNs). The mice were sacrificed on the 4th day, and the wound tissues were placed in saline by using ultrasonication to count the number of CFUs in the wound. The obtained solutions (100 μL) were plated onto LB agar plates and incubated at 37°C for 18 h. The wound tissues were harvested on therapeutic day 4 and fixed in 4% paraformaldehyde solution. Then the tissues were paraffin-embedded, sectioned, and analyzed by hematoxylin-eosin (H&E) staining and Masson's trichrome staining. All samples were examined using a microscope (Olympus IX-71).

CWSN Hemolysis Assay

A hemolysis assay was performed by using fresh animal blood from BALB/c mice. First, red blood cells (RBCs) were collected via centrifugation at 1500 rpm for 5 min and washed three times with PBS. RBC suspensions (0.1 mL) were added to 1 mL of different concentrations of CWSN saline dispersions (25, 50, 100, and 200 μg/mL). The mixtures were incubated at 37°C for 4 h. Ultrapure water and PBS were used as the positive control and negative control, respectively. Finally, the absorbance of the supernatant was measured at 540 nm after centrifugation at 12 000 rpm for 15 min.

Cytotoxicity Assay

CWSN cytotoxicity was evaluated using normal skin cells (HaCaT cells, human keratinocytes) by utilizing a lactate dehydrogenase (LDH) cytotoxicity assay and Calcein-AM/propidium iodide (Calcein-AM/PI) staining. HaCaT cells (10^4 cells/well) were added to 96-well plates. After 24 h, the supernatant medium was removed and CWSN dispersions (200 μL) containing different concentrations of CWSNs (25, 50, 100, and 200 μg/mL) were added to the wells. Wells supplemented with PBS were used as a control, and the cytotoxicity of CWSNs was determined according to the manufacturer's instructions.

Toxicity Study of CWSNs in vivo

Ten BALB/c mice were randomly divided into two groups (n = 5 /group) and i.v. injected with 200 μL of PBS and 200 μL of CWSNs (50 μg/mL) on day 0 and 5. All mice were sacrificed on the 25th day to obtain the major organs (heart, liver, spleen, lung, and kidney) for inductively coupled plasma–optical emission spectrometry (ICP-OES, Agilent 720ES, USA) analysis and H&E staining.

Statistical Analysis

In the present study, statistical analyses were performed using GraphPad Prism 8.0 (GraphPad Software, CA, USA). All data are presented as the means ± standard deviation (SD). Statistical differences between two groups were determined using the two-tailed Student's *t*-test. One-way or two-way ANOVA with multiple comparisons tests was performed as indicated. ns, not significant, $P > 0.05$; *$P < 0.05$; **$P < 0.01$; ***$P < 0.001$; ****$P < 0.0001$.

Results

Preparation and Characterization of CWSNs

The morphology of CWSNs is shown in Figure 1A, and the nanoparticle size distribution assessment showed that the CWSNs had an average size of ~20 nm (Figure 1B). The HRTEM images showed that the CWSNs had a cube-like appearances (Figure 1C) and that the crystal lattice of the CWSNs had a distance of approximately 0.495 nm (Figure 1D).

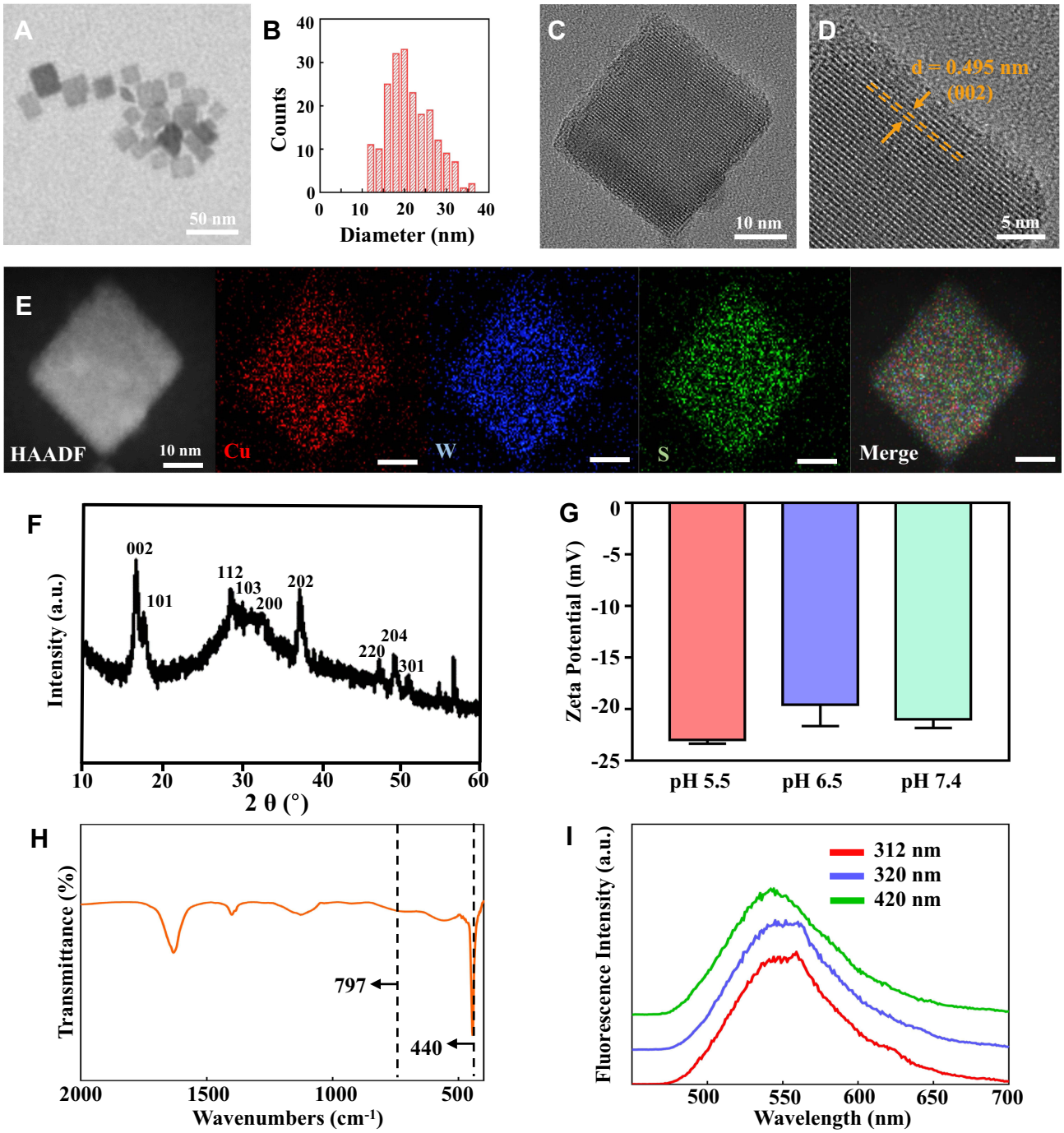

Figure 1 Characterization of the prepared CWSNs. (**A**) TEM image and (**B**) histogram of the CWSN size distribution. (**C** and **D**) HRTEM images of CWSNs, yellow arrows indicating crystal lattice of the CWSNs. (**E**) HAADF-STEM images of the CWSNs and elemental mapping images of Cu, W, and S. (**F**) XRD pattern of the CWSNs. (**G**) Zeta potentials of the CWSNs. (**H**) FTIR spectrum of the CWSNs. (**I**) Fluorescence emission spectra (excited at 312, 320, and 420 nm) of the CWSNs.
Abbreviations: CWSNs, Cu_2WS_4 nanocrystals; TEM, transmission electron microscopy; HRTEM, high-resolution TEM; XRD, X-ray diffraction.

Furthermore, the high-angle annular dark field scanning TEM (HAADF-STEM) images show that the CWSNs had a cubic morphology, and the corresponding EDS elemental mapping images show that elemental distributions of Cu, W, and S in the CWSNs (Figure 1E). The crystal structure of the CWSNs was characterized by XRD (Figure 1F). The zeta potentials of the CWSN preparations at different pH values were measured to be −23.0 ± 0.2, −19.6 ± 1.2, and −21 ± 0.6 mV at pH 5.5, 6.5 and 7.4, respectively (Figure 1G). Fourier transform infrared spectroscopy (FTIR) spectrum is shown in Figure 1H. All of these results indicate that the CWSNs were successfully prepared. In addition, the fluorescence spectra in Figure 1I show that the specific fluorescence peak of the CWSNs was found at a wavelength of ~550 nm by using different excitation wavelengths (312, 320, and 420 nm).

Photocatalytic Generation of •OH by CWSNs

Photocatalytic CWSNs can generate high levels of ROS (•OH) under visible-light irradiation; thus, photocatalytic CWSNs have potential antibacterial applications (Figure 2A). As shown in Figure 2B, the CWSN bandgap extraction is 2.45 eV. The VB was evaluated using UPS. Figure 2C shows that the VB position of the CWSNs is 4.51 eV. The conduction band (CB) of the CWSNs and •OH formation potential are shown in Figure 2D, which is specific for the CWSNs being suitable for generating •OH. Moreover, the generation of •OH was detected by using TA through fluorescence characterization in water under visible-light. Figure 2E shows that notable fluorescence intensity was generated through the production of •OH at a wavelength of 425 nm, indicating that the photocatalytic generation of •OH by the CWSNs had occurred.

Antibacterial Action of CWSNs in vitro

The antibacterial activity of the CWSNs was evaluated by using S. *aureus*. TEM and elemental mapping characterization were used to investigate CWSN antibacterial mode of action. TEM images (Figure 3A and B) show that CWSNs can adhere to the surfaces of *S. aureus* cells. HAADF-STEM-EDS elemental mapping images (Figure 3C) show that the

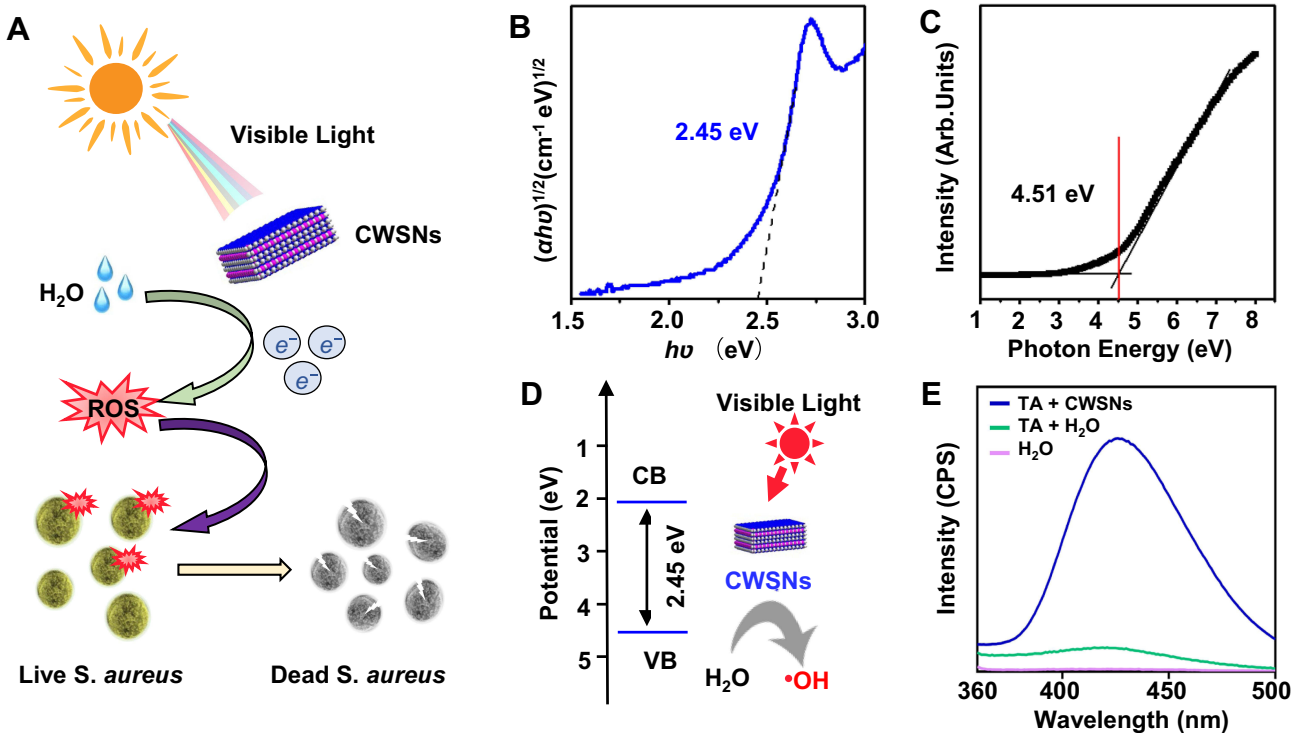

Figure 2 Photocatalytic induction of ROS formation by CWSNs. (**A**) Schematic showing the CWSN-mediated inactivation of bacteria through visible-light photocatalytic ROS generation. (**B**) Bandgap of the CWSNs, in which hυ is the photon energy and α is the absorption coefficient. (**C**) The VB edge of the CWSNs measured by using UPS. (**D**) Band position of the CWSNs with respect to ROS formation (OH•) potential. (**E**) Fluorescence spectra of TA with and without incubation with CWSNs.
Abbreviations: CWSNs, Cu_2WS_4 nanocrystals; ROS, reactive oxygen species; VB, valence band; CB, conduction band; UPS, ultraviolet photoelectron spectroscopy.

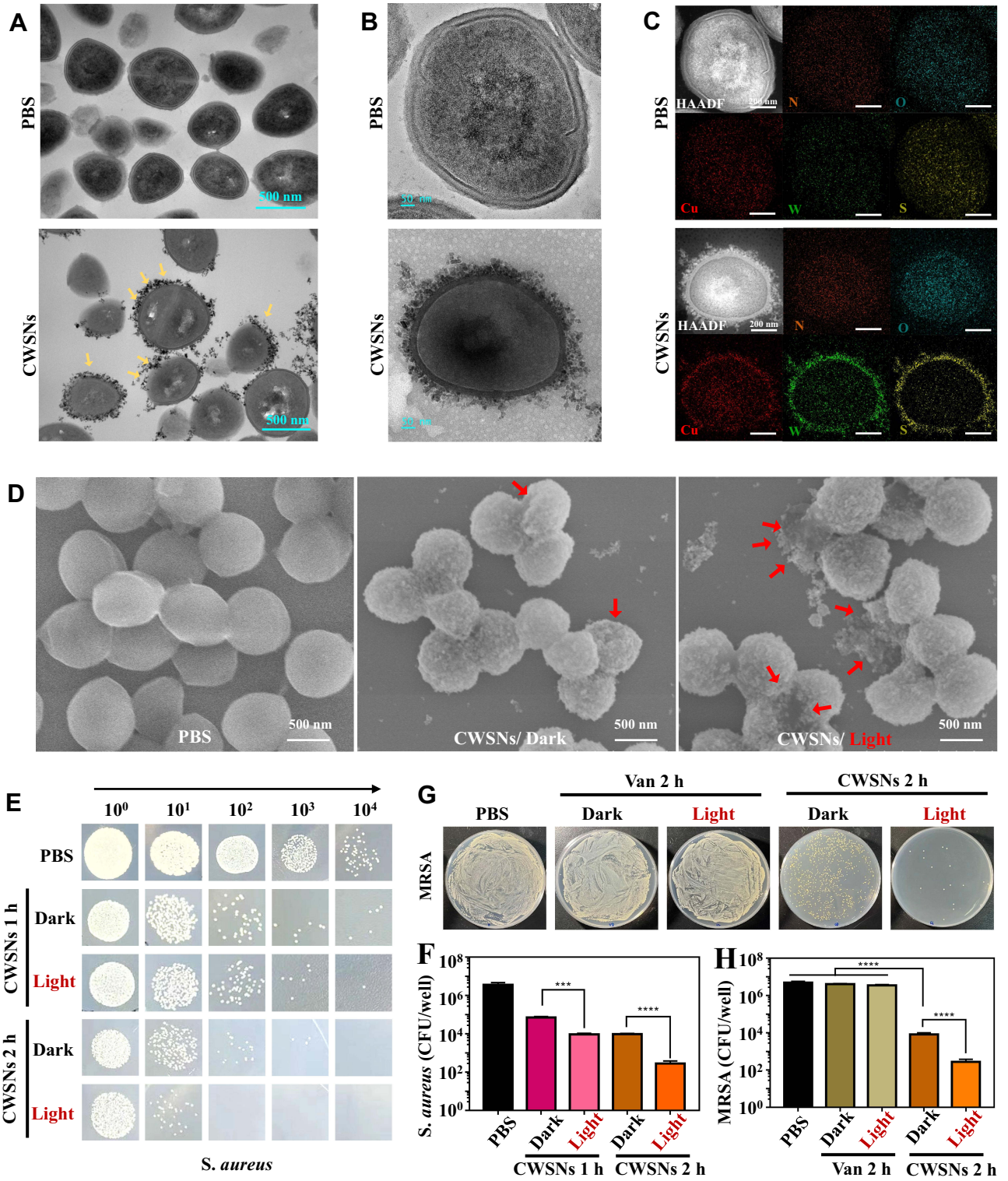

Figure 3 The antibacterial action of CWSNs in vitro. (**A** and **B**) Representative TEM images of PBS- and CWSN-treated *S. aureus* cells. Yellow arrows indicating bacteria-binding CWSNs. (**C**) Elemental mapping of *S. aureus* cells exposed to PBS or CWSNs. (**D**) SEM images of *S. aureus* treated with saline and 2 μg/mL CWSNs with or without visible-light stimulation. Red arrows indicating damaged and wrinkled *S. aureus*. (**E**) Original images and (**F**) CFU number of *S. aureus* after different treatments. (**G**) Photographs of bacterial broth plates and (**H**) bacterial viability of MRSA after treatment with 2 μg/mL Van or CWSNs. The statistical significance of differences between the indicated groups. ***$P < 0.001$, ****$P < 0.0001$.

strong Cu, W, and S signals mainly originate from the surfaces of the *S. aureus* cells, which suggests that CWSNs have a strong ability to bind to *S. aureus* cells. The bacterial morphology was also observed by scanning electron microscopy (SEM). The *S. aureus* cells cultured in saline (control) maintained a sphere-shaped morphology with intact and smooth cell membranes (Figure 3D), but those exposed to CWSNs became damaged and wrinkled. Moreover, the cells in the CWSNs plus visible-light group showed more visible structural damage than the cells treated in the dark. Furthermore, a low concentration of CWSNs (2 μg/mL) showed efficient *S. aureus* killing under both dark and visible-light conditions after 1 h of incubation, but the inactivation efficiency of CWSNs for *S. aureus* under visible-light irradiation was significantly higher than that in the dark after 2 h of incubation (Figure 3E and F). In addition, the MRSA inactivation efficiency of the CWSNs under visible-light was much higher than that of Van after 2 h, demonstrating the superior antibacterial efficacy of CWSNs compared with that of the identical concentrations of Van (Figure 3G and H). These results show that photocatalytic CWSNs under visible-light irradiation have a strong ability to kill free *S. aureus*.

Anti-Biofilm Potential of the CWSNs

Previous results have showed that CWSNs can excite ROS to inhibit biofilm potential formation under visible-light. The efficiency of CWSNs to inactivate *S. aureus* was studied under visible-light and in the dark using the plate count method. The biofilm biomass was analyzed by crystal violet staining as shown in Figure 4A. The biomass of the adhered biofilms

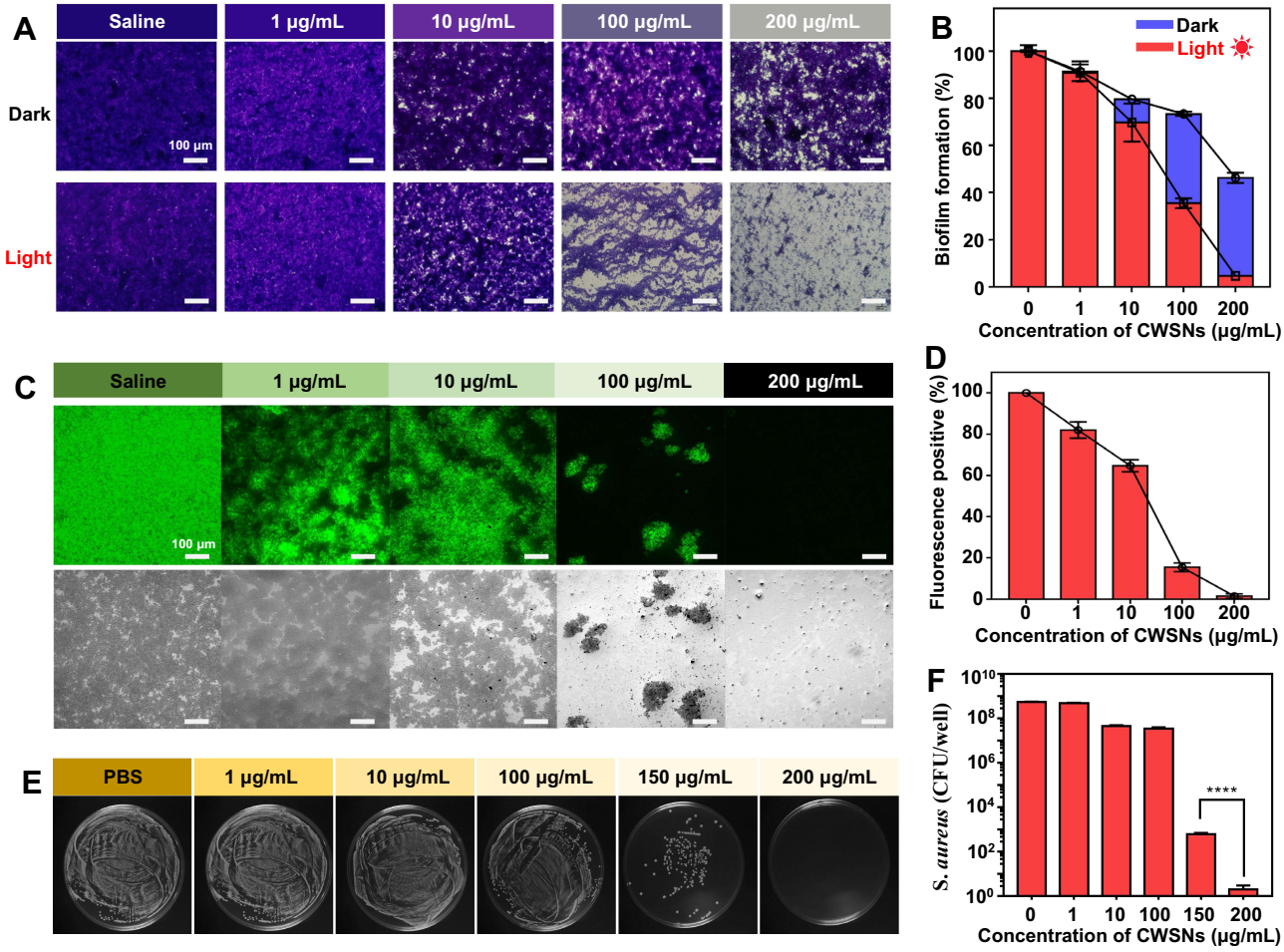

Figure 4 Inhibition of *S. aureus* biofilm formation. (**A**) Photograph of *S. aureus* biofilms after treatment with different concentrations of CWSNs followed by crystal violet staining. (**B**) Inactivation efficiency of *S. aureus* biofilms by CWSNs (1, 10, 100, and 200 μg/mL) under visible-light irradiation and in the dark. The biomass of the crystal violet-stained *S. aureus* biofilms was determined by measuring the absorbance at 590 nm. (**C**) CLSM images and (**D**) fluorescence quantification of the *S. aureus* biofilms after treatment with different concentrations of CWSNs. (**E**) Photographs of bacterial broth plates and (**F**) viability of *S. aureus* biofilms after treatment with different concentrations of CWSNs. The statistical significance of differences between the indicated groups. ****$P < 0.0001$.

decreased with increasing concentrations of CWSNs, and the biofilms were reduced up to ~97% at 200 μg/mL CWSNs under visible-light (Figure 4B). However, biofilms were reduced up to only ~46% after treatment with 200 μg/mL CWSNs in the dark. To investigate the antibiofilm potential of CWSNs under visible-light irradiation, we examined the efficiency of CWSNs to inhibit bacterial biofilms formation. Different concentrations of CWSNs were first added to each well of a 96-well plate, and then *S. aureus* in LB broth with glucose was added to the wells. After incubation for 24 h under static conditions, the biofilms clearly attached to the bare surface in the absence of CWSNs, while few biofilms formed with CWSN concentrations of 100–200 μg/mL. CLSM images further showed that the amount of adhered biofilm was dose-dependent (Figure 4C and D), which was consistent with the crystal violet staining results. As shown in Figure 4E, the number of CFUs of the *S. aureus* biofilms decreased with increasing concentrations of CWSNs. Figure 4F shows that the viability of the *S. aureus* biofilms exposed to CWSNs (200 μg/mL) decreased by approximately 100%, suggesting excellent antibiofilm activity. All of these results indicate that CWSNs can inhibit *S. aureus* biofilm formation.

CWSNs Promoted the Healing of Infected Wounds

To gain a better understanding of CWSN action on wounds, we generated different gels that were used to treat infected wounds (Figure 5A). Compared to the saline gel (control), the CWSN gel significantly inhibited the growth of bacteria on agar plates (Figure 5B). To evaluate the tissue regeneration and antibacterial activity of the CWSNs in vivo, a wound infection model was established on the backs of BALB/c mice (Figure 5C). The *S. aureus*-infected wounds were treated with both the saline gel and CWSN gel. The photographs show that the wounds in the CWSN gel-treated group were

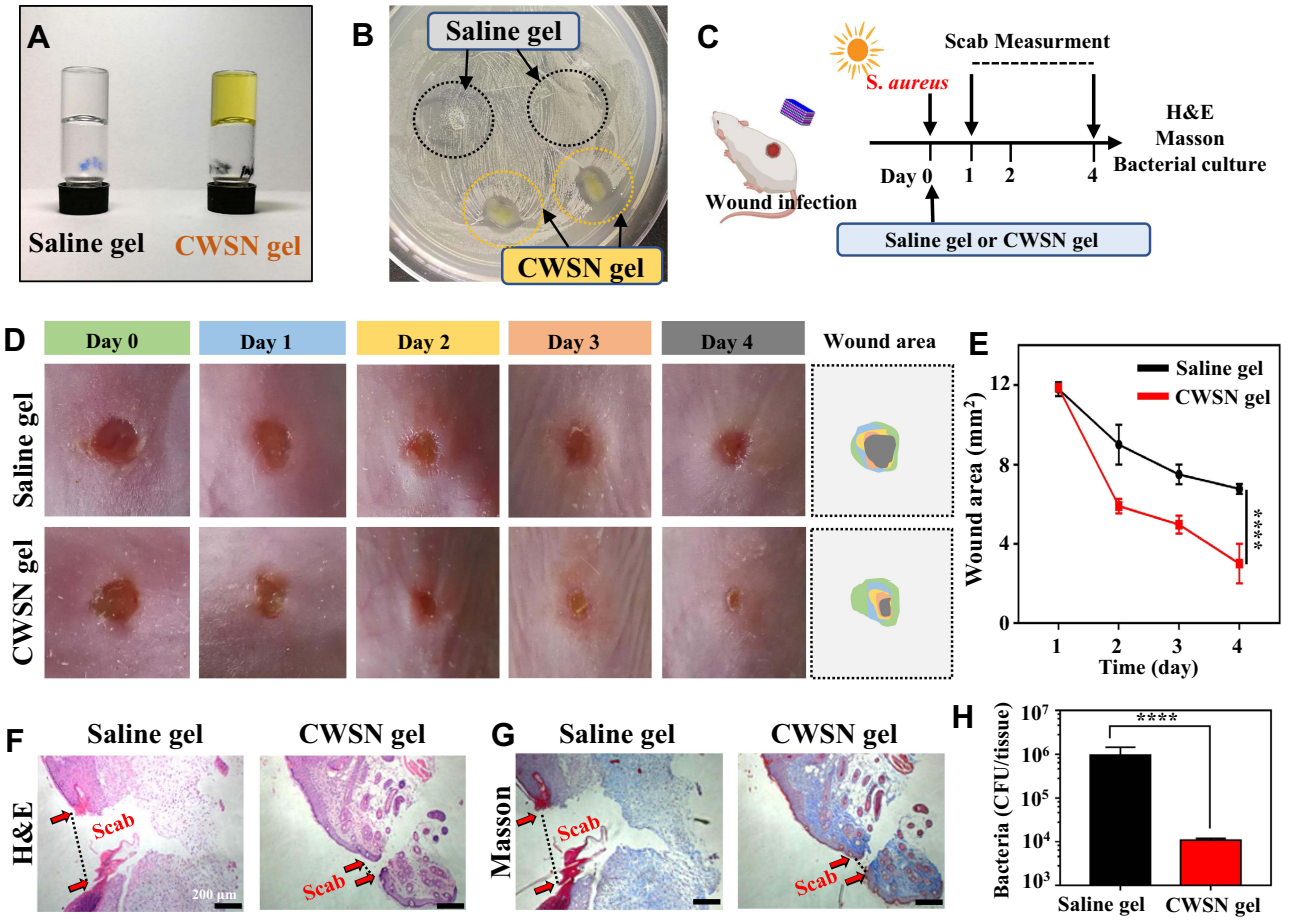

Figure 5 Treatment of *S. aureus*-infected wounds. (**A**) Photographs of the saline and CWSN gels. (**B**) Antibiofilm potential of the saline gel and CWSN gel in vitro. (**C**) Schematic diagram of the construction of the in vivo infection model and mouse treatment. (**D**) Photographs and (**E**) areas of the infected wounds on different days (0, 1, 2, 3 and 4) after saline gel or CWSN gel treatment. Microphotographs of the (**F**) H&E and (**G**) Masson's trichrome stained slices of *S. aureus*-infected tissues on the 4th day posttreatment. (**H**) Bacterial CFUs of the infected tissues 4 days after treatments. The statistical significance of differences between the indicated groups. ****$P < 0.0001$.

smaller than those in the saline group on the 3rd and 4th days (Figure 5D). Notably, the average wound area on the CWSN gel-treated mice was 3.81 mm^2, which was smaller than that of the saline gel-treated mice (average of 6.98 mm^2) on the 4th day, indicating that CWSNs can promote the healing of infected wounds (Figure 5E). The H&E and Masson staining results are shown in Figure 5F and G. The length of the epithelial gap in the CWSN gel-treated group was smaller than that in the saline gel group, and the mice in the saline gel group maintained clear scabbing and abundant neutrophils compared with the CWSN-treated group. Moreover, the bacterial inactivation efficiency of the CWSN gel-treated group was ~ 2 log units better than that of the saline gel group, suggesting that the CWSN gel can kill *S. aureus* in the infected wounds of mice (Figure 5H). All of these results indicate that CWSNs can efficiently treat *S. aureus*-infected wounds in mice and promote wound healing.

Biocompatibility of the CWSNs

Biocompatibility evaluations are essential for nanomaterials with potential biomedical applications. The colloidal stability of the CWSNs is illustrated in Figure 6A. The CWSNs showed limited aggregation after 24 h of incubation in different buffers. The hemolytic properties of the CWSNs were determined by using mouse erythrocytes. The CWSNs displayed a negligible hemolysis ratio even at high concentrations (up to 200 μg/mL), indicating that they have acceptable blood compatibility (Figure 6B). The cytotoxicity of the CWSNs was assessed with an LDH cytotoxicity assay using HaCaT cells. As shown in Figure 6C, the HaCaT cells remained >98% viable in the presence of the CWSNs at concentrations up to 200 μg/mL, indicating that CWSNs had limited toxicity. The confocal fluorescence results did not display any notable apoptotic cells (PI staining) after the HaCaT cells were co-incubated with different concentrations of CWSNs (Figure 6D). Furthermore, the long-term toxicity of the CWSNs to mice was studied. As shown in Figure 6E, the CWSNs were *i.v.* injected via the tail vein on days 0 and 5, and all mice were sacrificed on day 25. ICP-OES analysis of the major organs from the mice illustrated no clear Cu, W, or S deposition (Figure 6F–H). The H&E stained images of the major organs from the mice after two i.v. injection of CWSNs showed no noticeable damage or inflammatory lesions (Figure 6I). These results indicate that the CWSNs have excellent biosafety.

Discussion

Bacteria usually exist as biofilms, and biofilm-associated infectious diseases, such as chronic wound infections, pulmonary infections, endocarditis osteomyelitis, musculoskeletal infections, dental periodontitis, peri-implantitis, or even nosocomial infections, are an increasingly serious problem in the global medical community.[19–22] During the process of biofilm formation, bacteria attach to inert or biological surfaces and become wrapped in self-produced EPSs. EPSs have many negative effects, such as facilitating bacterial aggregation and biofilm cohesion, allowing cell–cell communication among the biofilm population and providing a source of nutrients. In addition, EPSs provide protection against both mechanical stresses and antibiotic treatments.[23] Thus, fighting bacterial biofilm-associated infections with traditional therapies is a major challenge. Therefore, there is an urgent need to develop novel treatment strategies that are effective at combating bacterial biofilms.

Nanomedicine has shown great promise for the diagnosis and therapy of various diseases.[24–26] In particular, nanomaterials have been extensively developed for the treatment of bacterial biofilm infections.[27–31] These antibiofilm nanomedicine technologies have many advantages; thus, an increasing number of antibiofilm agents have been ingeniously designed to eradicate the EPSs from the biofilms to kill the incorporated bacteria.[32–34] Recent studies have reported that novel photocatalytic antibiofilm nanoagents can possess photosensitive abilities or enzyme-like catalytic activities, which could disrupt the biofilm matrix and damage the bacterial cell components via the catalytic generation of ROS.[35–37] Therefore, developing novel photocatalytic antibiofilm nanomaterials is a promising treatment strategy for infectious diseases.

Ternary transitional metal sulfides possess a variety of intriguing chemical and physical properties and can be used in many fields. We successfully prepared CWSNs by a microwave irradiation method. The TEM results showed that CWSNs were small (average size of 20 nm). The HRTEM images showed that the crystal lattice distance of the CWSNs is approximately 0.495 nm, which corresponds to the (002) plane of *I*-CWS.[16] The crystal structure of the CWSNs was characterized by XRD, and the diffraction peaks can be attributed to the *I*-CWS planes. In addition, the zeta-potential results indicated that the CWSNs are negatively charged in pH 5.5~7.4 solution. From the FTIR results, a series of peaks

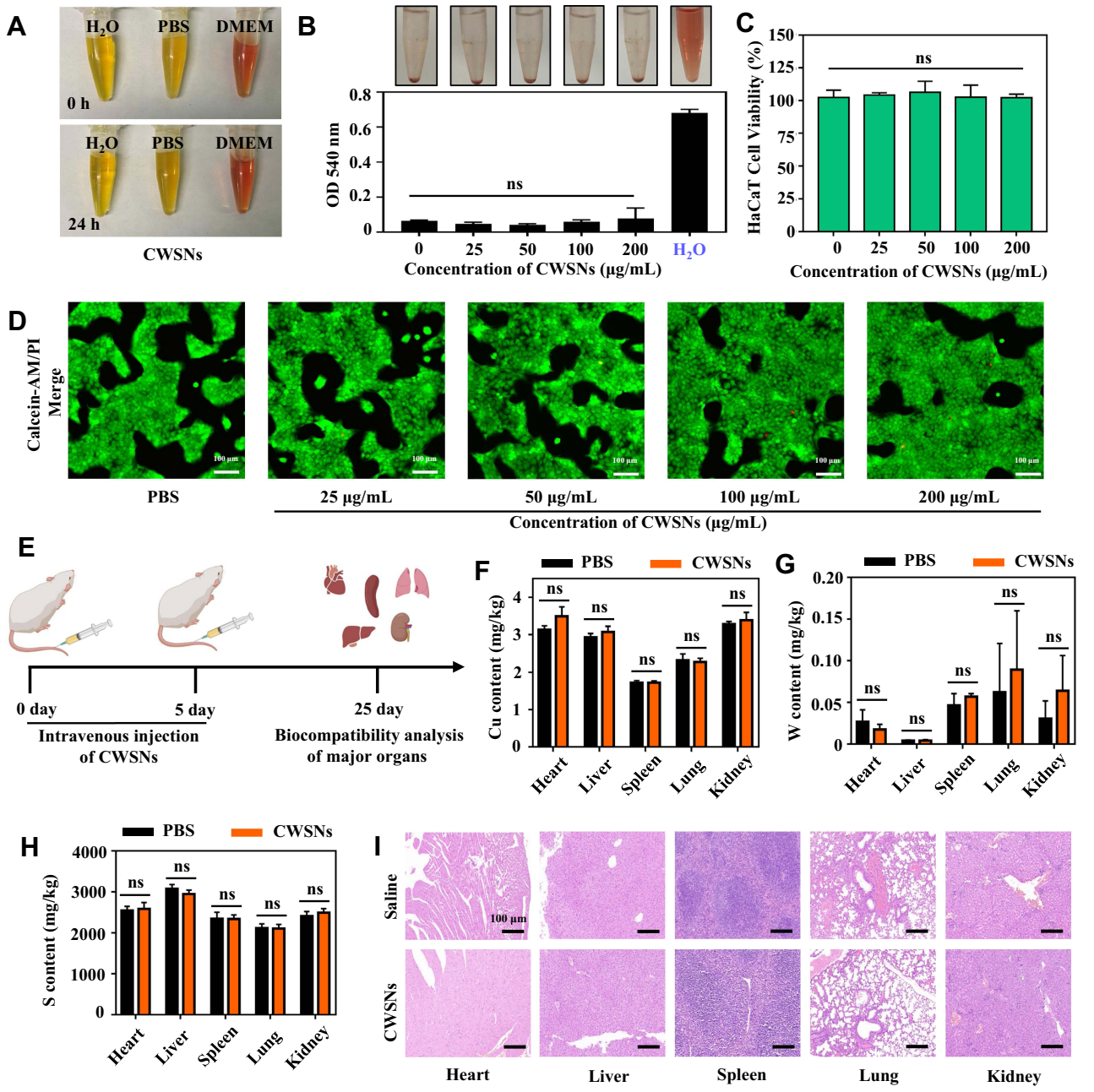

Figure 6 Biocompatibility of the CWSNs. (**A**) Photographs of the CWSNs dispersed in H_2O, PBS, and DMEM at different time points. (**B**) Hemolysis ratio of fresh red blood cells (RBCs) incubated with different concentrations of CWSNs for 4 h. (**C**) Viability (%) of HaCaT cells after co-cultured with different concentrations of CWSNs. (**D**) CLSM images of HaCaT cells stained with Calcein-AM/PI after treatment with different concentrations of CWSNs. (**E**) Schematic illustration of the experimental procedure for determining the cytotoxicity of CWSNs in vivo. ICP-OES results for the element deposition of (**F**) Cu, (**G**) W, and (**H**) S, and (**I**) H&E stained images of the major organs (heart, liver, spleen, lung, and kidney) from the mice treated with saline and CWSNs at 25 days. The statistical differences between the indicated groups. ns, not significant.

at approximately 797 cm^{-1} and 946 cm^{-1} were assigned to the characteristic vibrations of CWSNs.[38] Visible-light is a mixture of different wavelengths, and particular wavelengths are important for the excitation of photoactive compounds. The specific fluorescence peak of CWSNs was found at a wavelength of ~550 nm by using different excitation wavelengths (312, 320, and 420 nm).

A previous study demonstrated that Cu_2WS_4 nanocrystals have oxidase- and peroxidase-like activities that are involved in ROS production.[18] The UV–vis diffuse reflectance spectrum suggested that the as-synthesized I-Cu_2WS_4 submicron crystallites had a direct bandgap of approximately 2.15 eV. The as-synthesized I-Cu_2WS_4 submicron

crystallites exhibited considerably high photocatalytic activity for the reduction of aqueous Cr (VI) under visible-light ($\lambda > 420$ nm) irradiation.[39] Herein, the bandgap of the CWSNs was extracted from the relationship between the photon energy and absorption coefficient based on the UV–vis-NIR absorption spectrum.[18] Compared with reported CWS materials, characterization of the CWSN properties demonstrated that the bandgap and VB of CWSNs were 2.45 eV and 4.51 eV, respectively, which enables the CWSNs to generate •OH for bacterial inactivation;[39] in addition, the bandgap of CWSNs is larger than that of CWS materials, which may due to their smaller size. Moreover, the generation of •OH was detected by using TA fluorescence detection in water under visible-light. The TA fluorescence spectra showed that CWSNs can generate a large amount of •OH under visible-light. Notably, •OH, a highly toxic ROS, can kill bacteria by destroying essential macromolecules and inducing oxidative lesions in the bacterial membrane.[40]

S. aureus is a common nosocomial bacterium that can cause different infections, from those on the skin and in soft tissue infections to those that are more serious and life-threatening, such as sepsis.[41,42] The TEM images showed that the CWSNs can adhere to the surfaces of *S. aureus* cells, which suggests that they may interact with some specific components on the bacterial surface. Bacteria cell walls contain peptidoglycan consisting of amino acid residues, which may coordinate to the metal ions in the CWSNs. After CWSN treatment, elemental mapping images revealed that the surfaces of the *S. aureus* cells became rough. The HAADF-STEM-EDS elemental mapping images showed that the strong Cu, W, and S signals mainly originated from the surfaces of the *S. aureus* cells, which suggests that the CWSNs have a strong ability to bind to *S. aureus* cells. The bacteria-binding ability of the CWSNs can facilitate the attachment of nanozymes to the bacteria surface and decrease the diffusion distance of the released •OH, which will greatly facilitate bacterial killing by •OH.[18] In the present study, the photocatalytic CWSNs showed high antibacterial activity after treatment for 2 h at a low concentration (2 μg/mL). The SEM images showed that the CWSNs can adhere to the *S. aureus* cell membranes and cause damage and the appearance of wrinkles in the membrane structure, especially in a visible-light environment. In addition, CWSNs (2 μg/mL) exhibited a higher inactivation efficiency of *S. aureus* within 2 h of incubation under visible-light than after incubation in the dark. Furthermore, a low concentration of CWSNs (2 μg/mL) efficiently killed MRSA. More interestingly, the efficiency of the CWSNs to inactivate *S. aureus* was higher than that of the commonly used antibiotic Van (2 μg/mL). Therefore, photocatalytic CWSNs possess excellent antibacterial activity due to their bacteria-binding ability and photocatalytic generation of •OH.

In addition, as antibiofilm nanomaterials, photocatalytic CWSNs can effectively inhibit *S. aureus* biofilms formation. Thus, the biofilms biomass decreased with increasing concentrations of CWSNs. Studies on the properties of the CWSNs have demonstrated these nanomaterials can catalyze the generation of •OH under visible-light. The biofilms were reduced up to ~38% at 100 μg/mL or ~97% at 200 μg/mL CWSNs under visible-light. However, biofilms were reduced up to only 72% at 100 μg/mL or ~46% at 200 μg/mL CWSNs in the dark. Under visible-light conditions, the CLSM images showed that the biofilms were notably destroyed after exposure to a sufficient concentration of CWSNs (200 μg/mL). Moreover, the CFUs of the *S. aureus* biofilms decreased with increasing concentrations of CWSNs. Compared to the bactericidal effect of against free bacteria, biofilm disruption requires a higher concentration of CWSNs due to the protection from the EPSs.[43] These results demonstrated that CWSNs have excellent antibacterial properties and can promote biofilm disruption in vitro.

It is difficult for traditional nanoagent solutions to remain on a wound for a long time. Thus, there is a great need for new administration approaches, such as the use of a gel, which is a convenient method with many advantages, including controlled release performance, biodegradability and biocompatibility. The results showed that the CWSN gel was successfully prepared and had a remarkable antibacterial effect plates covered with *S. aureus*. To evaluate the antibacterial activity of the CWSN gel in vivo, a wound infection model was established on the backs of BALB/c mice according to a previous method.[44] The in vivo data showed that the CWSN gel achieved an ~2 log unit improvement in bacterial inactivation efficiency in *S. aureus*-infected mice and efficiently promoted wound healing. The H&E and Masson staining results showed that the length of the epithelial gap in the CWSN gel-treated group was smaller than that in the saline gel-treated group. Furthermore, the saline gel group continued to display notable scabbing and abundant neutrophils compared with the CWSN gel-treated group. Therefore, the above results indicate that the CWSN gel not only inhibited the bacteria but also promoted tissue regeneration and had excellent wound healing abilities.

It is essential to evaluate the toxicity of nanoagents prior to their applications in biomedicine. CWSNs at different concentrations (25, 50, 100, and 200 μg/mL) were cultivated with HaCaT cells for 24 h. The results of the LDH assay

demonstrated that the CWSNs had almost no cytotoxicity toward HaCaT cells in vitro, which indicated that CWSNs had acceptable biocompatibility. Copper and sulfur are essential elements in the human body, and ionic tungsten species have low bioaccumulation and can be excreted from the body through feces and urine. The ICP-OES results showed no obvious element deposition (Cu, W, and S) in mice after CWSN treatment in vivo. Furthermore, after i.v. injection of CWSNs into mice, the photomicrographs of the major organs showed no abnormalities at 25 days, which indicates that the CWSNs have excellent biocompatibility.

This work provides a photocatalytic nanoagent to potentially inhibit bacterial or even drug-resistant bacterial biofilm formation with good biocompatibility.

Conclusion

Overall, CWSNs were prepared for the efficient killing S. *aureus* and inhibition of biofilm formation via photocatalytically generating •OH under visible-light irradiation. The CWSN gel displayed excellent efficacy to inactivate *S. aureus* in vivo and promoted infected wound healing. This work provides an emerging photocatalytic nanomaterial for efficient bacterial killing, inhibition of biofilms growth and wound infection treatment.

Acknowledgments

We also greatly appreciate the support from Dr. Lihui Yuwen (Nanjing University of Posts and Telecommunications). The authors also want to thank AJE for professional English language editing, and BioRender for providing drawing elements, which helped visualize our research. The authors appreciate the kind support of Shiyanjia Lab (www.shiyanjia.com) for the TEM Characterization.

Funding

This research was funded by the National Natural Sciences Foundation of China (81371680), and Jiangsu Provincial Medical Talent (ZDRCC2016016), Key Project of Research and Development Plan of Jiangsu Province (BE2020629), and Development of Science and Technology of Nanjing (YKK19094).

Disclosure

The authors declare no conflicts of interest in this work.

References

1. Iwase T, Uehara Y, Shinji H, et al. Staphylococcus epidermidis Esp inhibits Staphylococcus aureus biofilm formation and nasal colonization. *Nature*. 2010;465(7296):346–349. doi:10.1038/nature09074
2. Foster TJ, Geoghegan JA, Ganesh VK, et al. Adhesion, invasion and evasion: the many functions of the surface proteins of Staphylococcus aureus. *Nat Rev Microbiol*. 2014;12(1):49–62. doi:10.1038/nrmicro3161
3. Li Y, Xiu W, Yang K, et al. A multifunctional Fenton nanoagent for microenvironment-selective anti-biofilm and anti-inflammatory therapy. *Materials Horizons*. 2021;8(4):1264–1271. doi:10.1039/D0MH01921F
4. Wang Z, Liu X, Duan Y, et al. Infection microenvironment-related antibacterial nanotherapeutic strategies. *Biomaterials*. 2022;280:121249. doi:10.1016/j.biomaterials.2021.121249
5. Flemming HC, Wingender J. The biofilm matrix. *Nat Rev Microbiol*. 2010;8(9):623–633. doi:10.1038/nrmicro2415
6. Wani FA, Bandy A, Alenzi MJS, et al. Resistance patterns of gram-negative bacteria recovered from clinical specimens of intensive care patients. *Microorganisms*. 2021;9(11):2246. doi:10.3390/microorganisms9112246
7. Xiu W, Shan J, Yang K, et al. Recent development of nanomedicine for the treatment of bacterial biofilm infections. *View*. 2021;2(1):20200065. doi:10.1002/VIW.20200065
8. Wang LS, Gupta A, Rotello VM. Nanomaterials for the treatment of bacterial biofilms. *ACS Infect Dis*. 2016;2(1):3–4. doi:10.1021/acsinfecdis.5b00116
9. Lv X, Zhang J, Yang D, et al. Recent advances in pH-responsive nanomaterials for anti-infective therapy. *J Mater Chem B*. 2020;8(47):10700–10711. doi:10.1039/D0TB02177F
10. Cao C, Zhang T, Yang N, et al. POD nanozyme optimized by charge separation engineering for light/pH activated bacteria catalytic/photodynamic therapy. *Signal Transduct Target Ther*. 2022;7(1):86. doi:10.1038/s41392-022-00900-8
11. Shan J, Zhang X, Kong B, et al. Coordination polymer nanozymes-integrated colorimetric microneedle patches for intelligent wound infection management. *Chem Eng J*. 2022;444:136640. doi:10.1016/j.cej.2022.136640
12. Yang Y, Wang C, Wang N, et al. Photogenerated reactive oxygen species and hyperthermia by Cu_3SnS_4 nanoflakes for advanced photocatalytic and photothermal antibacterial therapy. *J Nanobiotechnology*. 2022;20(1):195. doi:10.1186/s12951-022-01403-y

13. Wang W, Li G, Xia D, et al. Photocatalytic nanomaterials for solar-driven bacterial inactivation: recent progress and challenges. *Environ Sci Nano*. 2017;4(4):782–799.
14. Liu C, Kong D, Hsu P-C, et al. Rapid water disinfection using vertically aligned MoS_2 nanofilms and visible light. *Nat Nanotechnol*. 2016;11(12):1098–1104. doi:10.1038/nnano.2016.138
15. Tao J, Luttrell M, Fau-Batzill T, Batzill M. A two-dimensional phase of TiO_2 with a reduced bandgap. *Nat Chem*. 2011;3(4):296–300. doi:10.1038/nchem.1006
16. Ozel F, Aslan E, Sarilmaz A, et al. Hydrogen evolution catalyzed by Cu_2WS_4 at liquid-liquid interfaces. *ACS Appl Mater Interfaces*. 2016;8(39):25881–25887. doi:10.1021/acsami.6b05582
17. Li N, Liu M, Zhou Z, et al. Charge separation in facet-engineered chalcogenide photocatalyst: a selective photocorrosion approach. *Nanoscale*. 2014;6(16):9695–9702. doi:10.1039/C4NR02068E
18. Shan J, Li X, Yang K, et al. Efficient bacteria killing by Cu(2)WS(4) nanocrystals with enzyme-like properties and bacteria-binding ability. *ACS Nano*. 2019;13(12):13797–13808. doi:10.1021/acsnano.9b03868
19. Nguyen TH, Cheung GYC, Rigby KM, et al. Rapid pathogen-specific recruitment of immune effector cells in the skin by secreted toxins. *Nat Microbiol*. 2022;7(1):62–72. doi:10.1038/s41564-021-01012-9
20. de Sousa TA-O, Hébraud M, Dapkevicius MLNE, et al. Genomic and metabolic characteristics of the pathogenicity in Pseudomonas aeruginosa. *Int J Mol Sci*. 2021;22(23):12892. doi:10.3390/ijms222312892
21. Dong H, Liu H, Zhou N, et al. Surface modified techniques and emerging functional coating of dental implants. *Coatings*. 2020;10(11):1012. doi:10.3390/coatings10111012
22. Cao C, Ge W, Yin J, et al. Mesoporous silica supported silver-bismuth nanoparticles as photothermal agents for skin infection synergistic antibacterial therapy. *Small*. 2020;16(24):e2000436. doi:10.1002/smll.202000436
23. Blackman LD, Qu Y, Cass P, et al. Approaches for the inhibition and elimination of microbial biofilms using macromolecular agents. *Chem Soc Rev*. 2021;50(3):1587–1616. doi:10.1039/D0CS00986E
24. Dong H, Wen Z-F, Chen L, et al. Polyethyleneimine modification of aluminum hydroxide nanoparticle enhances antigen transportation and cross-presentation of dendritic cells. *Int J Nanomedicine*. 2018;13:3353–3365. doi:10.2147/IJN.S164097
25. Park S-M, Aalipour A, Vermesh O, et al. Towards clinically translatable in vivo nanodiagnostics. *Nat Rev Mater*. 2017;2(5):17014. doi:10.1038/natrevmats.2017.14
26. Liu H, Dong H, Zhou N, et al. SPIO enhance the cross-presentation and migration of DCs and anionic SPIO influence the nanoadjuvant effects related to interleukin-1beta. *Nanoscale Res Lett*. 2018;13(1):409. doi:10.1186/s11671-018-2802-0
27. Xiu W, Gan S, Wen Q, et al. Biofilm microenvironment-responsive nanotheranostics for dual-mode imaging and hypoxia-relief-enhanced photodynamic therapy of bacterial infections. *Research*. 2020;2020:9426453. doi:10.34133/2020/9426453
28. Shi LA-O, Zhao Y, Xie Q, et al. Moldable hyaluronan hydrogel enabled by dynamic metal-bisphosphonate coordination chemistry for wound healing. *Adv Healthc Mater*. 2018;7(5):1700973. doi:10.1002/adhm.201700973
29. Talemi AK, Jalali A, Mohammadi A, et al. The Fe3O4 nanoparticles functionalized by glutamic acid and conjugated with thiosemicarbazide decreases the expression of icaA and icaD biofilm genes in methicillin-resistant Staphylococcus aureus isolates. *Gene Rep*. 2022;26:101515. doi:10.1016/j.genrep.2022.101515
30. Montazeri A, Salehzadeh A, Zamani H. Effect of silver nanoparticles conjugated to thiosemicarbazide on biofilm formation and expression of intercellular adhesion molecule genes, icaAD, in Staphylococcus aureus. *Folia Microbiol*. 2020;65(1):153–160. doi:10.1007/s12223-019-00715-1
31. Honarmand T, Sharif AP, Salehzadeh A, et al. Does conjugation of silver nanoparticles with thiosemicarbazide increase their antibacterial properties? *Microb Drug Resist*. 2022;28(3):293–305. doi:10.1089/mdr.2020.0557
32. Li X, Shan J, Zhang W, et al. Recent advances in synthesis and biomedical applications of two-dimensional transition metal dichalcogenide nanosheets. *Small*. 2017;13(5):1602660. doi:10.1002/smll.201602660
33. Wang Q, Zhang Y, Li Q, et al. Therapeutic applications of antimicrobial silver-based biomaterials in dentistry. *Int J Nanomed*. 2022;17:443–462. doi:10.2147/IJN.S349238
34. Zhang Y, Xiu W, Gan S, et al. Antibody-functionalized MoS_2 nanosheets for targeted photothermal therapy of staphylococcus aureus focal infection. *Front Bioeng Biotechnol*. 2019;7:218. doi:10.3389/fbioe.2019.00218
35. Wainwright M, Maisch T, Nonell S, et al. Photoantimicrobials-are we afraid of the light? *Lancet Infect Dis*. 2017;17(2):e49–e55. doi:10.1016/S1473-3099(16)30268-7
36. Wu S, Xu C, Zhu Y, et al. Biofilm-sensitive photodynamic nanoparticles for enhanced penetration and antibacterial efficiency. *Adv Funct Mater*. 2021;31(33):2103591. doi:10.1002/adfm.202103591
37. Shan J, Yang K, Xiu W, et al. Cu_2MoS_4 nanozyme with NIR-II light enhanced catalytic activity for efficient eradication of multidrug-resistant bacteria. *Small*. 2020;16(40):e2001099. doi:10.1002/smll.202001099
38. Peng D, Wang Y, Shi H, et al. Fabrication of novel $Cu_2WS_4/NiTiO_3$ heterostructures for efficient visible-light photocatalytichydrogen evolution and pollutant degradation. *J Colloid Interface Sci*. 2022;613:194–206. doi:10.1016/j.jcis.2021.10.179
39. Jia Q, Zhang YC, Li J, et al. Hydrothermal synthesis of Cu_2WS_4 as a visible-light-activated photocatalyst in the reduction of aqueous Cr(VI). *Mater Lett*. 2014;117:24–27. doi:10.1016/j.matlet.2013.11.110
40. Sun H, Gao N, Dong K, et al. Graphene quantum dots-band-aids used for wound disinfection. *ACS Nano*. 2014;8(6):6202–6210. doi:10.1021/nn501640q
41. Idrees M, Sawant S, Karodia N, et al. Staphylococcus aureus biofilm: morphology, genetics, pathogenesis and treatment strategies. *Int J Environ Res Public Health*. 2021;18(14):7602. doi:10.3390/ijerph18147602
42. Coimbra AA-O, Miguel S, Ribeiro M, et al. Thymus zygis essential oil: phytochemical characterization, bioactivity evaluation and synergistic effect with antibiotics against Staphylococcus aureus. *Antibiotics*. 2022;11(2):146. doi:10.3390/antibiotics11020146
43. Prażmo EJ, Godlewska RA, Mielczarek AB. Effectiveness of repeated photodynamic therapy in the elimination of intracanal Enterococcus faecalis biofilm: an in vitro study. *Lasers Med Sci*. 2017;32(3):655–661. doi:10.1007/s10103-017-2164-3
44. Yuwen L, Sun Y, Tan G, et al. MoS_2@polydopamine-Ag nanosheets with enhanced antibacterial activity for effective treatment of Staphylococcus aureus biofilms and wound infection. *Nanoscale*. 2018;10(35):16711–16720. doi:10.1039/C8NR04111C